Supporting Information

Albert et al. 10.1073/pnas.1716305114

SI Materials and Methods

Cell Culture. *Chlamydomonas reinhardtii mat3-4* cells (strain CC-3994) (49), which exhibit superior vitrification due to their small size, were acquired from the *Chlamydomonas* Resource Center, University of Minnesota, St. Paul. Cells were grown until mid-log phase in Tris-acetate-phosphate (TAP) medium under constant light exposure (~90 μmol photons m^{-2} s^{-1}) and bubbling with normal atmosphere.

Cell Vitrification and Cryo-FIB Milling. Vitrification and FIB sample preparation were performed as previously described (16, 50). Using a Vitrobot Mark 4 (FEI), cells in suspension (4 μL of ~1,000 cells per microliter) were blotted onto R2/1 carbon-coated 200-mesh copper grids (Quantifoil Micro Tools) and plunge frozen in a liquid ethane/propane mixture. Grids were then mounted into Autogrid supports (FEI) and transferred into either a FEI Scios or FEI Quanta dual-beam FIB/SEM instrument. The grids were coated with an organometallic platinum layer by the gas injection system (FEI), and cells were thinned from both sides with a gallium ion beam to a final thickness of ~100–200 nm.

Cryo-ET. Cellular tomograms were acquired on a 300 kV Titan Krios microscope (FEI), equipped with a Gatan postcolumn energy filter (968 Quantum) and a direct detector camera (K2 summit, Gatan) operated in movie mode at 12 frames per second. Tilt series were recorded in SerialEM software (51) with 2° tilt increments from approximately −60° to +60° (in two halves separated at either 0° or −20°), an object pixel size of 3.42 Å, a defocus of −4 to −5.5 μm, and a total accumulated dose of <100 e^{-}/Å.

Tomogram Reconstruction. Frames from the K2 detector were drift corrected with MotionCor2 software (52) using 3 × 3 patches. Using IMOD software (53), tilt series were aligned with patch tracking, and tomograms were reconstructed with weighted back projection. Tilts of poor quality, judged by patch tracking alignment scores and inspection of the power spectrum, were omitted from the reconstruction. Only tomograms with high-quality alignments and power spectrums were further analyzed, reducing our initial dataset from ~130 to 76 tomograms. Most of these tomograms were acquired from separate cells, from several different cell cultures. To enhance the tomogram contrast in Figs. 1 and 4 and Movie S1, we used the tom_deconv deconvolution filter (https://github.com/dtegunov/tom_deconv).

Proteasome Template Matching. Proteasome positions were determined by template matching (54) twice-binned tomograms (13.68-Å pixel size) with PyTom software (55). The template was a low-pass filtered 20S core particle attached to one 19S regulatory particle, produced by masking one cap of a double-capped proteasome single particle cryo-EM structure (Electron Microscopy Data Bank: EMD-2165) (23). This template produced strong hits for both single-capped and double-capped proteasomes within our tomograms. High cross-correlation peaks were extracted from within the cellular volumes, and the corresponding subtomograms were visually screened for the presence of proteasomes.

Proteasome Subtomogram Averaging and Classification. Initial subtomogram averages were calculated with PyTom software (55) and consisted of 3,322 particles from 76 tomograms. To exclude template bias, the subvolumes were first aligned globally with spherical harmonics (56) and then refined in local angular space with real space alignment. As an additional control, the subvolumes were subjected to reference-free alignment with spherical harmonics (Fig. S1). Refinement of subtomogram averages was performed with Relion software (57), including internal normalization and contrast transfer function (CTF) correction with CTFFIND4 (58). Final polishing was accomplished by restricting the tilt series to a range of −30° to +30°. Resolution was determined in Relion by gold-standard Fourier shell correlation (FSC) (Fig. S1).

The dataset was processed through multiple rounds of autofocused 3D classification (AC3D) (59) in PyTom, as diagrammed in Fig. S1. The number of classes in each round was oversampled and then hierarchically clustered to detect small subpopulations. The first round sorted assembly states, separating single-capped from double-capped 26S proteasomes, while also removing false positives. Proteasomes were then cut in half, and each of the 5,498 halves was handled as a distinct particle. Further classifications sorted the halves into two 19S functional states (ground and substrate-processing states) and three 19S binding states (free, basket-tethered, and membrane-tethered).

Fitting of Molecular Models. Using rigid-body fitting in UCSF Chimera software (60), a molecular model of the S1 ground-state proteasome (26) was fit into the EM densities of the basket-tethered and membrane-tethered subtomogram averages, enabling visualization of where the extra densities contact the proteasome.

Proteasome Distance and Orientation Analysis. To estimate the distances of proteasomes to the nuclear envelope, the twice-binned tomograms were segmented into five regions: (*i*) complete cellular volume, (*ii*) nucleoplasm, (*iii*) nuclear envelope, (*iv*) nuclear pores, and (*v*) cytoplasm. Distance-dependent concentrations of nuclear and cytoplasmic proteasomes (Fig. 1*F*) were calculated by counting proteasomes in concentric shells (of equal radii and known volume) that expanded from the nuclear envelope into both the nucleoplasm and cytoplasm.

With nearest neighbor analysis, we calculated the orthogonal distances of both the proteasome centers (20S core, Fig. S7*A*) and tips (Rpn9 subunit, Fig. 3*A*) to the INM. Orientations to the INM (Fig. S7*B*) were measured by the angle between the proteasome long axis and the membrane's orthogonal vector. Distances to the closest NPC (Fig. 3*A* and Fig. S7*C*) were measured by the lateral distance of the proteasome tip to the orthogonal vector from the NPC center. The inclination of each proteasome to its closest NPC (Fig. S7*D*) was measured by the angle between the proteasome long axis and the vector extending from the NPC center to the proteasome center. For above measurements involving NPCs, only NPCs that were >20% contained within the tomogram volume were considered to more accurately determine the NPC centers and orthogonal vectors.

For heatmaps of radial proteasome positions around the NPC (Fig. 3*B*), proteasome tip positions (centered on Rpn9) were plotted in relation to one NPC asymmetric unit by placing spheres with 5 pixel radii into the volume. To visualize the distribution around the full NPC, the resulting heatmap was symmetrized eightfold and normalized to the number of proteasomes in each binding state class, thus showing the probability of proteasome localization per pixel. For this analysis, only NPCs with >75% of their structures contained within the tomogram volume were considered, and the angles and shifts from the subtomogram average of the NPC asymmetric unit were used.

Nuclear Pore Complex Subtomogram Averaging. Positions for 78 NPCs with >75% of their structures contained within the tomogram volume were picked during segmentation of the twice-binned tomograms. As a first step, subvolumes were manually aligned so that the nuclear and cytoplasmic sides of the NPCs were correctly oriented. An initial average of the whole NPC was calculated with PyTom software (55), exploiting the complex's eightfold symmetry. Using this symmetrized average, each NPC's 8 asymmetric units were subsequently identified and extracted, yielding 624 asymmetric units. Alignment and averaging of these asymmetric units were carried out using the AV3/TOM packages as described in ref. 61. The cytoplasmic, nuclear, and inner ring of each asymmetric unit were further aligned independently, as described in ref. 62. To assemble a complete NPC model, structures of the asymmetric unit were stitched together with eightfold symmetry (Fig. S8).

Data Availability. All subtomogram averages presented in this study have been deposited in the Electron Microscopy Data Bank (EMD-3932, EMD-3933, EMD-3934, EMD-3935, EMD-3936, EMD-3937, EMD-3938, EMD-3939, and EMD-3940), along with the tomogram from Fig. 1 (EMD-3967).

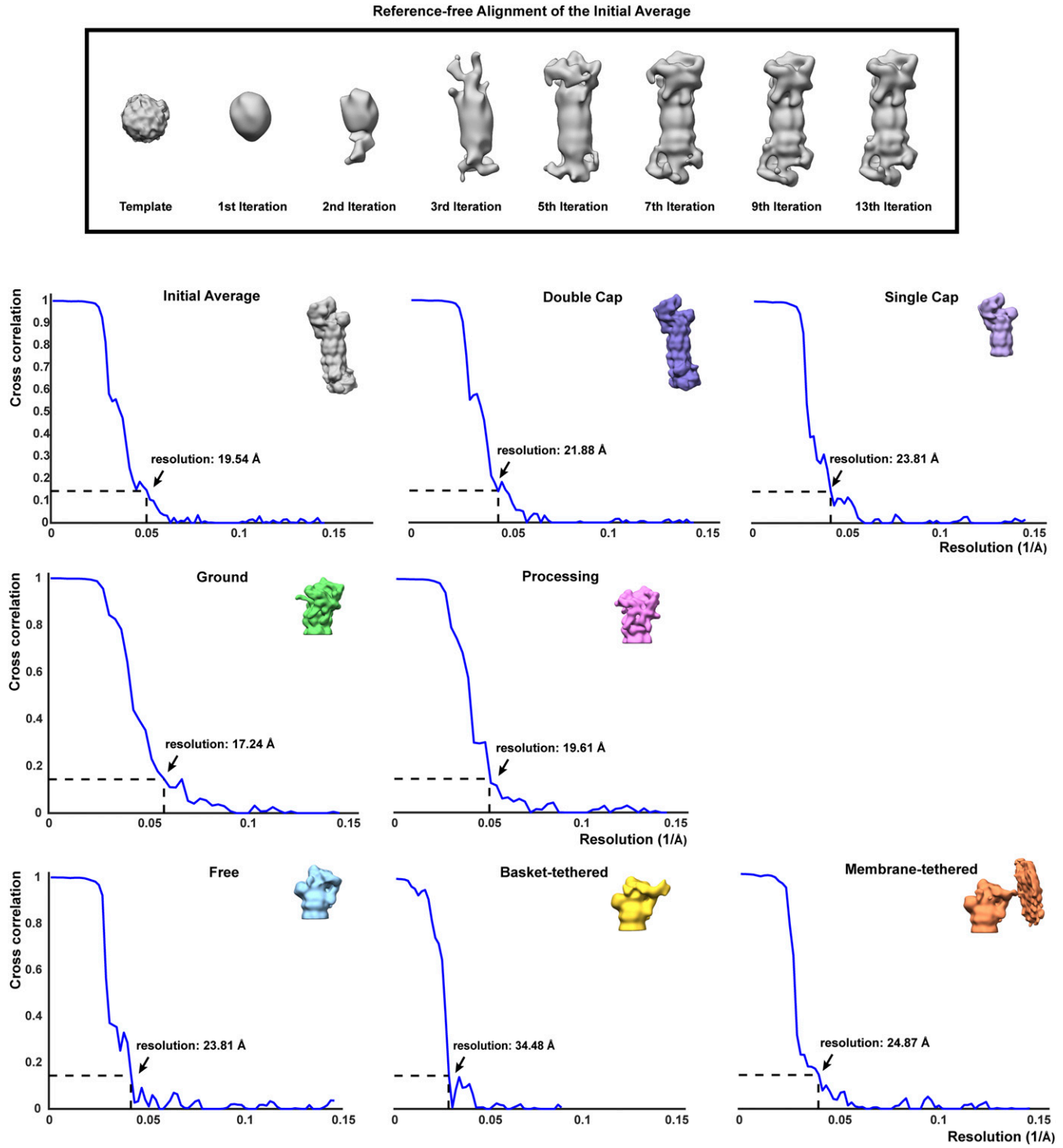

Fig. S1. Spherical harmonics reference-free alignment of the initial global average of all proteasomes (*Top* row) and Fourier shell correlation (FSC) curves for the in situ subtomogram averages of each classified proteasome state. (*Second* row) Initial average and averages of assembly states. (*Third* row) Averages of functional states. (*Bottom* row) Averages of binding states. All FSC curves were calculated by gold-standard assessment in Relion (63). The resolution was determined by the 0.143 cutoff criterion (dashed lines).

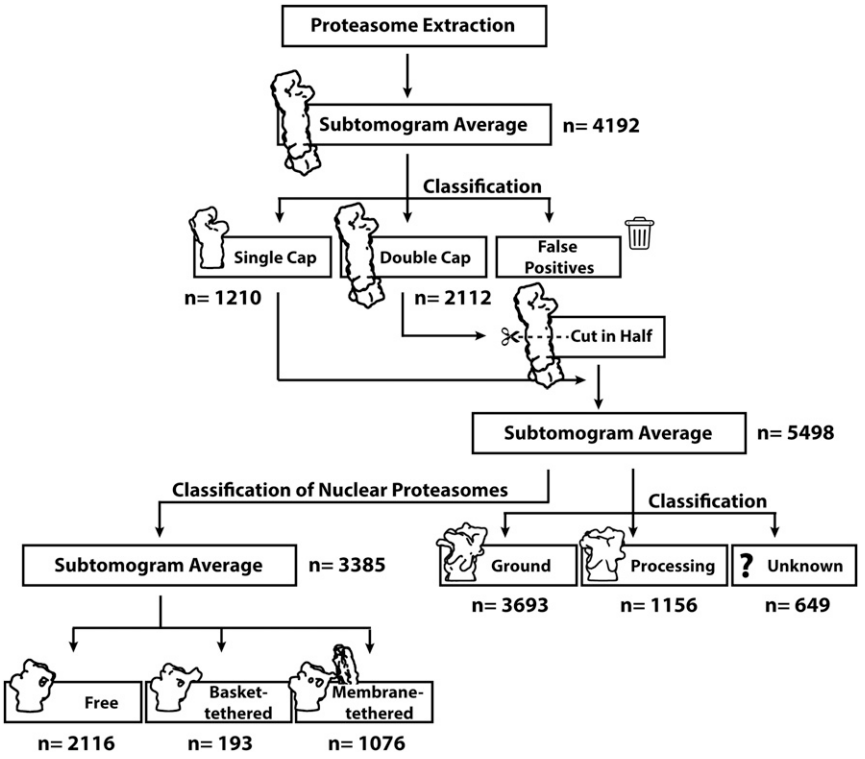

Fig. S2. Proteasome classification tree used to produce the structures in Fig. 2. An initial subtomogram average of the 4,192 volumes extracted from template matching was classified into single-capped and double-capped proteasomes, as well as false positives, which were discarded from the dataset. The 2,112 double-capped proteasomes were cut in half and both halves merged with the 1,210 single-capped proteasomes. The resulting average of 5,498 proteasome halves was further classified in two separate parallel trees. The functional states were classified into 3,693 ground-state caps, 1,156 substrate-processing state caps, and 649 caps that could not be identified beyond doubt. Whereas cytoplasmic proteasomes showed no further diversity, 3,385 nuclear proteasome halves could be classified into 2,116 free caps, 193 basket-tethered caps, and 1,076 membrane-tethered caps. To refine all of the classes, several iterations were performed at each classification step.

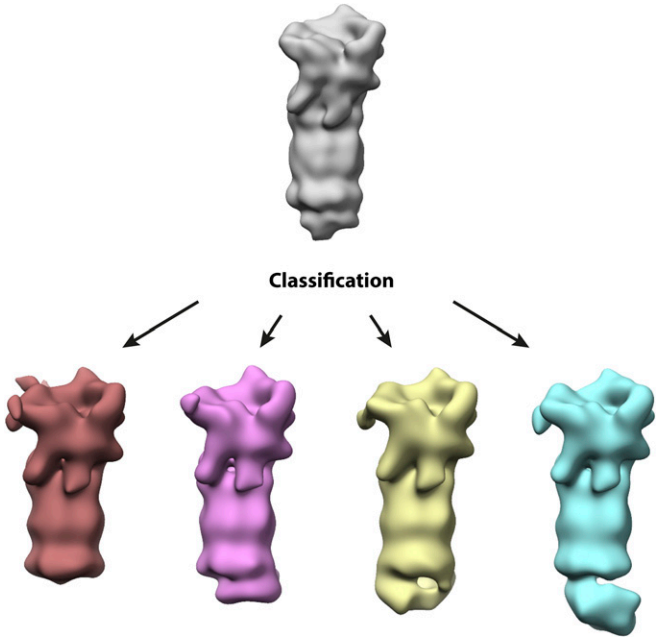

Fig. S3. Classification revealed heterogeneous density on the side of single-capped proteasomes that lack a 19S particle. The density on this side of the proteasome is highly variable and could correspond to a mix of 19S assembly states and the Blm10 complex (3).

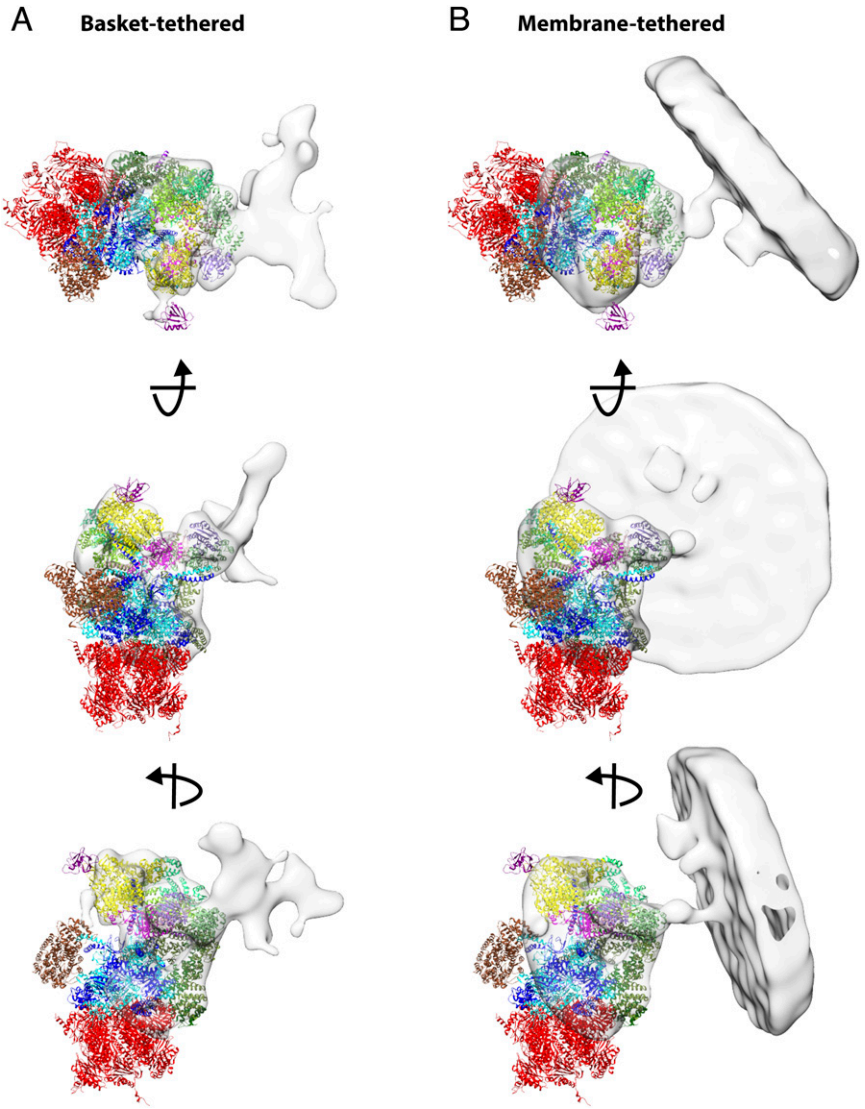

Fig. S4. Refined tether structures from focused alignment of the (*A*) basket-tethered and (*B*) membrane-tethered classes. (*Top* row) Top view and (*Middle* and *Bottom* rows) side views. Arrows indicate rotation between views. The EM maps were rigidly fit with a molecular model of the ground-state proteasome (26). Both extra densities bind to similar locations on Rpn9 (light green). This figure accompanies Fig. 2 *E* and *F*.

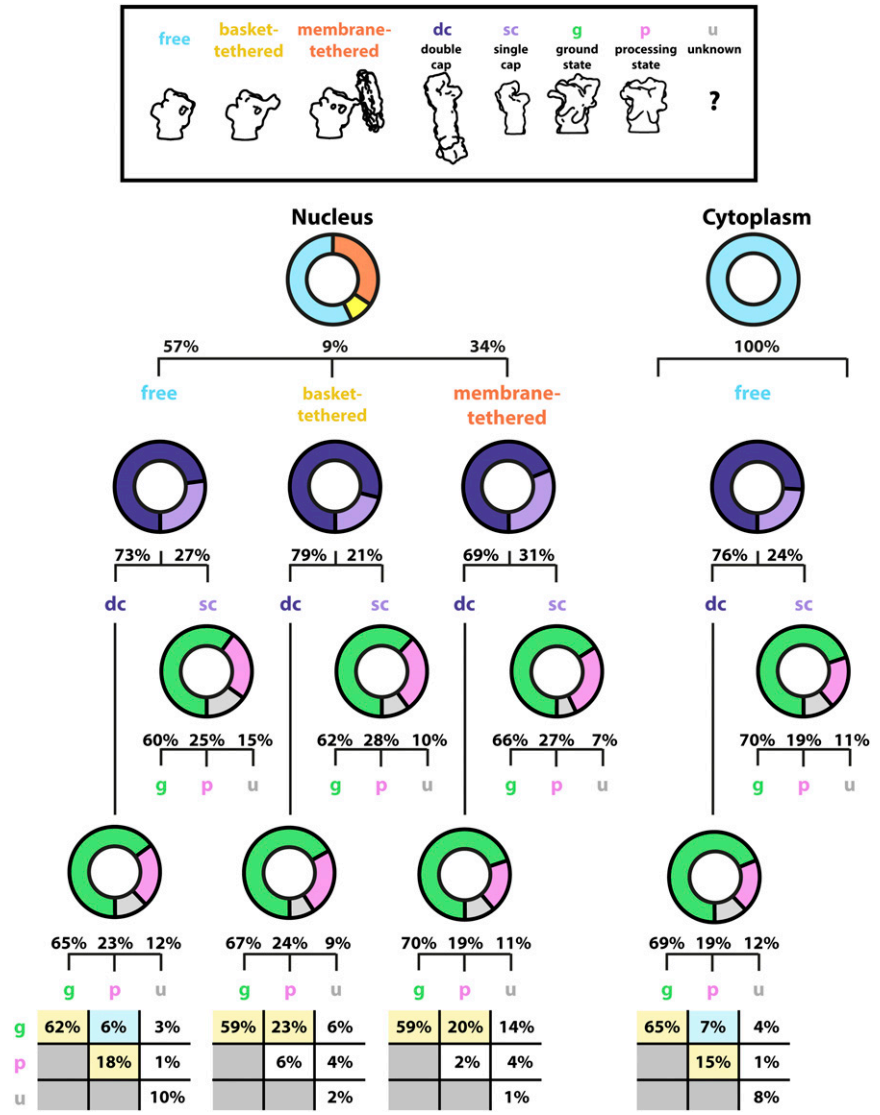

Fig. S5. Detailed population statistics of nuclear and cytoplasmic proteasomes. Proteasomes are divided hierarchically first by nuclear or cytoplasmic localization, then by binding state, then by assembly state, and finally by 19S functional state. The 19S particles of double-capped proteasomes can each assume different functional states, but we observed higher (yellow boxes) and lower (blue boxes) percentages for some combinations of functional states than what would be expected for uncorrelated caps. Color and naming key for the classes is indicated in the *Top* box. This figure accompanies Fig. 2*D*.

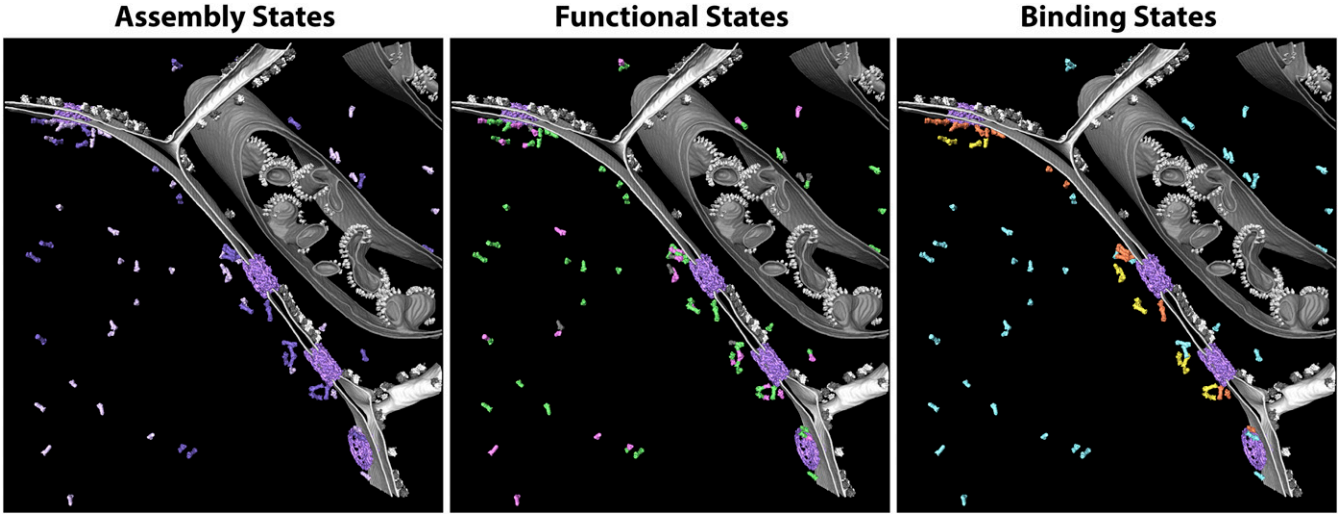

Fig. S6. Mapping each of the different proteasome states into cellular volumes. From *Left* to *Right*, the images show the tomogram segmentation from Fig. 1*B* populated with assembly states (double-capped, dark purple and single-capped, lavender), functional states (ground state, green; substrate-processing state, pink; and unknown, dark gray), and binding states (free, light blue; basket-tethered, yellow; and membrane-tethered, orange). Basket-tethered and membrane-tethered binding states are exclusively found near NPCs (purple). This figure accompanies Movie S1.

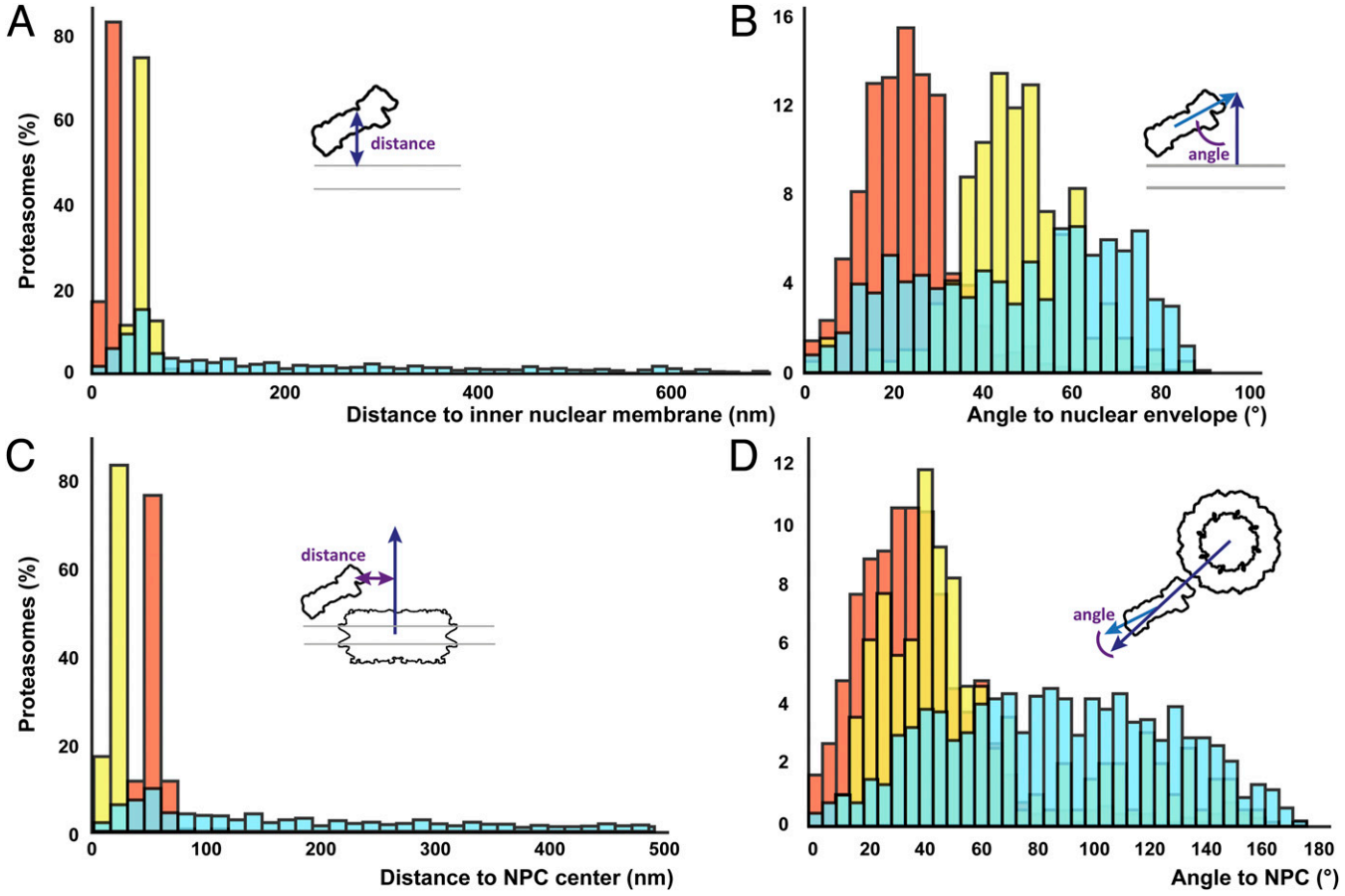

Fig. S7. Quantification of proteasome positions and orientations, classified by binding state. Blue, free; yellow, basket-tethered; and orange, membrane-tethered. (*A*) Proteasome distance to the INM, measured from the 20S center. Averages ± SD: 53.2 ± 9.1 nm for basket-tethered and 18.8 ± 3.8 nm for membrane-tethered. (*B*) Inclination of proteasomes to the INM. (*C*) Lateral distances between proteasome Rpn9 subunits and NPC centers. (*D*) Orientations of proteasomes relative to NPCs, measuring the angle between the proteasome long axis and a vector from the NPC center.

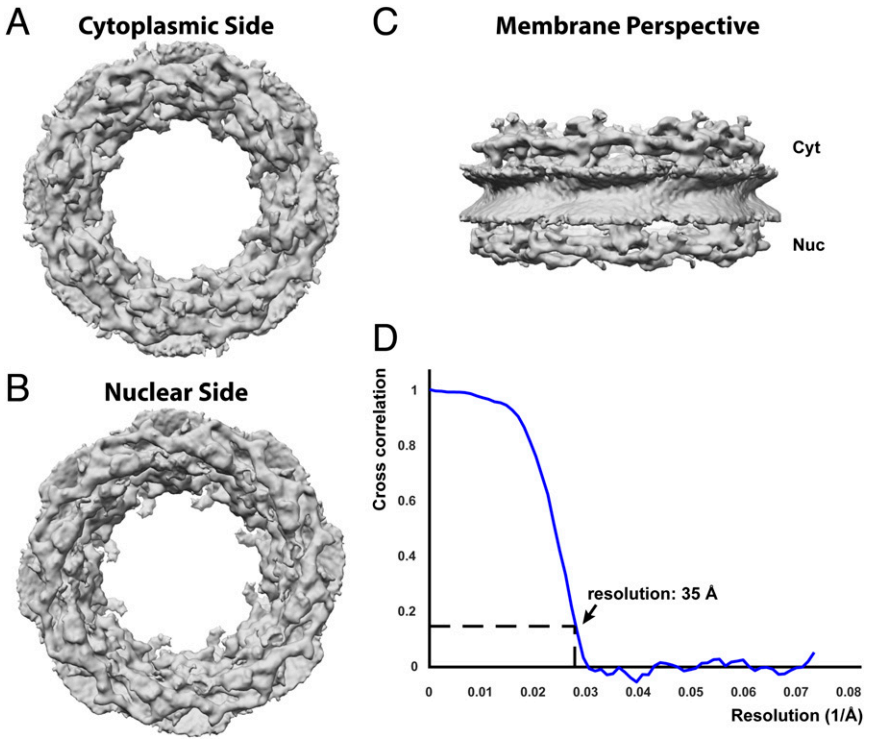

Fig. S8. In situ subtomogram average of the *Chlamydomonas* NPC. The average was calculated from 78 NPCs that had >75% of their total area contained within the cellular volume. To compensate for flexibility of the pore structure, alignment was performed on the asymmetric unit. The asymmetric units were then stitched together according to the NPC's eightfold symmetry. (*A*) Cytoplasmic face, (*B*) nuclear face, (*C*) perspective along the nuclear envelope (Cyt, cytoplasmic ring; Nuc, nuclear ring), and (*D*) FSC curve calculated by gold-standard assessment in Relion (63), showing a resolution of 35 Å at the 0.143 cutoff criterion.

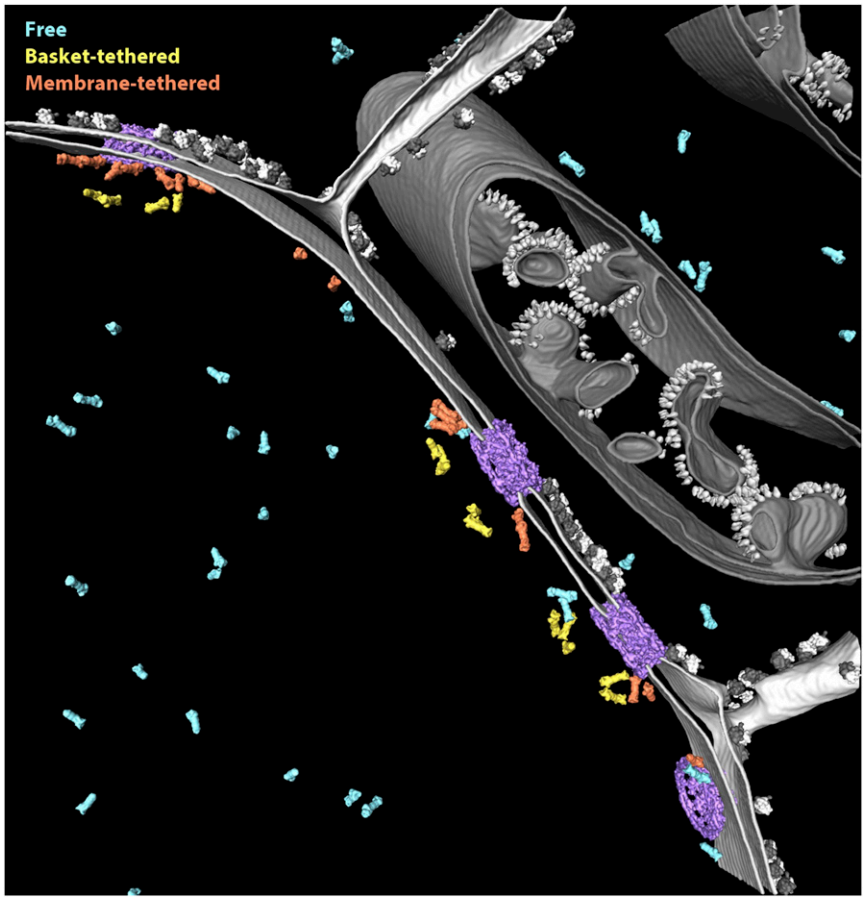

Movie S1. Sequential sections back and forth through the tomographic volume shown in Fig. 1*A* (orthographic view), followed by reveal of the 3D segmentation from Fig. 1*B* (perspective view). Each class of assembly states, functional states, and binding states is then mapped into the cellular volume, as in Fig. S6.

Movie S1

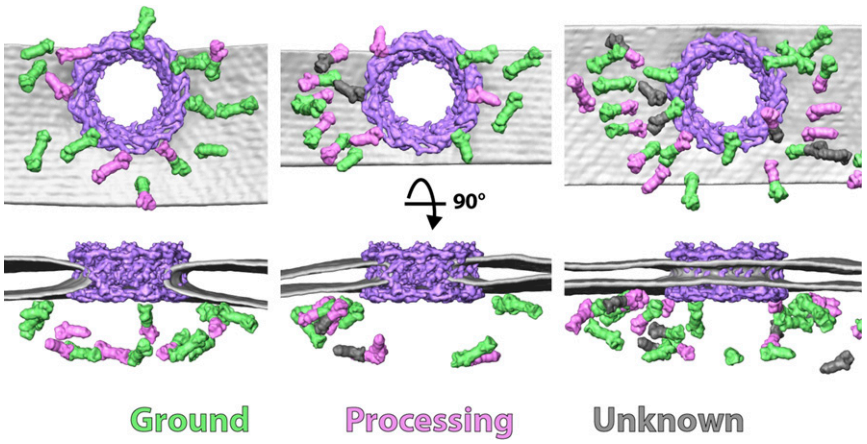

Movie S2. Orthographic nuclear views of NPCs (purple) showing double-capped (dark purple) and single-capped (lavender) assembly states, followed by ground (green), substrate-processing (pink), and unknown (dark gray) functional states, followed by free (light blue), basket-tethered (yellow), and membrane-tethered (orange) binding states. This movie accompanies Fig. 3*C*.

Movie S2